Twisted chiral superconductivity in photodoped frustrated Mott insulators

Jiajun Li,[1, 2] Markus Müller,[1] Aaram J. Kim,[2] Andreas M. Läuchli,[1, 3] and Philipp Werner[2]

[1]*Laboratory for Theoretical and Computational Physics,*
Paul Scherrer Institute, 5232 PSI Villigen, Switzerland
[2]*Department of Physics, University of Fribourg, 1700 Fribourg, Switzerland*
[3]*Institute of Physics, École Polytechnique Fédérale de Lausanne (EPFL), 1015 Lausanne, Switzerland*

Recent advances in ultrafast pump-probe spectroscopy provide access to hidden phases of correlated matter, including light-induced superconducting states, but the theoretical understanding of these nonequilibrium phases remains limited. Here we report how a new type of chiral superconducting phase can be stabilized in photodoped frustrated Mott insulators. The metastable phase features a spatially varying order parameter with a 120° phase twist which breaks both time-reversal and inversion symmetry. Under an external electric pulse, the 120° chiral superconducting state can exhibit a second-order supercurrent perpendicular to the field in addition to a first-order parallel response, similar to a nonlinear anomalous Hall effect. This phase can be tuned by artificial gauge fields when the system is dressed by high-frequency periodic driving. The mechanism revealed in this study applies to Mott insulators on various frustrated lattices and the hidden superconducting phase can be realized in both cold-atom quantum simulators and correlated solids.

The last decades have witnessed an intensive search for superconducting states with spontaneously broken time-reversal and inversion symmetry. Historically the first proposal involved chemically doped Mott insulating states of high-T_c copper oxides, although the predicted properties have not been detected in experiments [1]. Since then the tantalizing chiral superconducting state, an essential building block for topological quantum computers, has been sought after in various systems, such as Sr_2RuO_4 [2], UPt_3 [3, 4] and lately also in twisted bilayer graphene [5]. In the meantime, advances in cold-atom experiments and ultrafast spectroscopy have enabled the exploration of metastable hidden states of correlated systems, which are not accessible via a thermal pathway [6–9]. A remarkable phenomenon is the putative light-induced superconductivity, which has been observed in the vicinity of Mott insulating phases [10–13]. One promising route to such hidden phases is photodoping, where the laser excitation drastically redistributes charges by simultaneously creating long-lived particle-like (doublon) and hole-like (holon) charge carriers [14–18]. With low enough entropy, the photocarriers may form a BEC-like superconducting condensate [12] supported by the doublon-holon exchange mediated by virtual charge recombination processes [19–22]. It is thus tempting to ask whether a chiral superconducting state can be realized as a hidden phase in photodoped Mott insulators.

Here we use state-of-the art numerical simulations to demonstrate that a chiral superconducting state with a 120° phase twist can be stabilized by photodoping Mott insulators on frustrated lattices. The non-equilibrium nature of photodoped quasiparticles endows them with an exchange term of positive sign, an important ingredient favoring chiral condensates especially on frustrated lattices [23]. The 120° order has been discussed in noncollinear antiferromagnets and Floquet-driven bosonic systems [24]. Here instead we consider a fermionic condensate exhibiting an exotic supercurrent response that requires no or little Floquet engineering. Remarkably, the 120° superconducting phase features a spatially varying order parameter and persistent currents which change handedness under the inversion or time-reversal transformation, even in the absence of an external magnetic field. The condensate is found to prevail in an extended parameter regime, and can be further enhanced by artificial gauge fields created by periodic driving [25–27]. We confirm the existence of this ordered hidden phase on a Bethe lattice with infinite coordination number using nonequilibrium dynamical mean-field theory, and on the triangular and Kagome lattices using exact diagonalization. The exotic order may be realized in fermionic cold-atom systems and Kagome-lattice correlated materials, such as herbertsmithite [28], where its stability can be tuned through Floquet-engineered artificial gauge fields. It may also be relevant for the light-induced superconducting state observed in κ–$(BEDT–TTF)_2Cu[N(CN)_2]Br$ [12].

Doublon-holon condensate on three-colorable lattices

We consider a half-filled fermionic Hubbard model under external driving, focusing on the triangular, the Kagome, and the Bethe lattice, see Fig. 1. All these lattices are 3-colorable (we use the color labels R, G, B) and consist of connected RGB chains or loops, i.e., triangular motifs. The Hamiltonian reads

$$H = -t_0 \sum_{\langle ij \rangle \sigma} e^{i\varphi_{ij}} c_{i\sigma}^{\dagger} c_{j\sigma} + U \sum_i n_{i\uparrow} n_{i\downarrow} + g H_{\mathrm{dr}}, \quad (1)$$

where $c_{i\sigma}$ is the electron annihilation operator at site i with spin σ, $\langle ij \rangle$ denotes nearest-neighbor pairs, and t_0 and $U > 0$ are hopping and interaction parameters. The
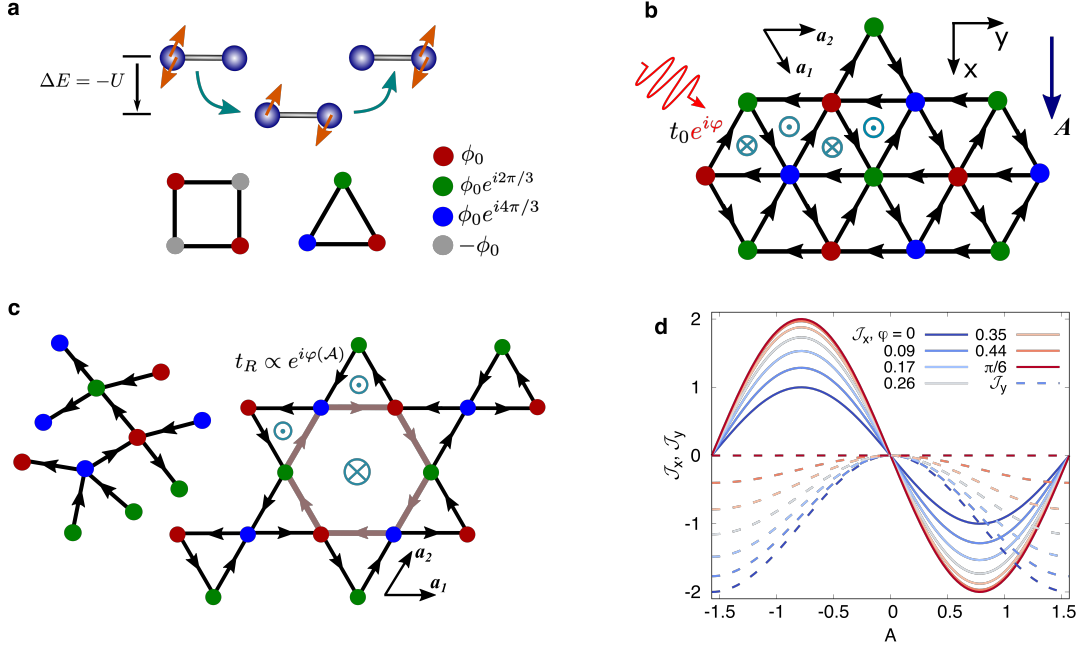
FIG. 1. **Doublon-holon condensate on a three-colorable frustrated lattice.** The persistent currents are indicated by black arrows. A high-frequency driving (red wavy line in panel (b)) induces an artificial gauge field coupling to the hopping t_0 through the Peierls phase φ, resulting in a flux (indicated by a dot and cross) for the triangular and hexagonal motifs in panels (b) and (c). (a) The doublon-holon exchange interaction mediated by a virtual recombination. The amplitude $J_\perp$ is positive, in contrast to analogous processes in the equilibrium attractive Hubbard model. It can induce staggered η–pairing on bipartite lattices and $120°$ pairing on three-colorable lattices. (b) The condensate on the triangular lattice. $\boldsymbol{a}_{1,2}$ are the basis vectors of the lattice. This panel also shows a constant vector potential along the x–direction. (c) The condensates on the Bethe (left) and Kagome (right) lattices. One of several possible $120°$ condensates (the $\boldsymbol{q} = 0$ order) is shown for the Kagome lattice. The magnitude of the flux through the hexagon is twice that of a triangle. (d) The longitudinal ($\mathcal{J}_x$, solid lines) and transverse ($\mathcal{J}_y$, dashed lines) superconducting current density under the constant vector potential $\boldsymbol{A}$ along the x–direction for the triangular lattice (with $A = 2|\boldsymbol{A}|\cos(\pi/6)$), see panel (b). φ is given in radians.

Peierls phases φ_{ij} represent an artificial gauge field implemented through a periodic (Floquet) modulation [25, 26]. As will be demonstrated below, the gauge field can be used to tune the superconducting (SC) condensate's stability, but the twisted condensate also exists for $\varphi = 0$ on the triangular and Bethe lattices. To realize a long-lived photodoped state, we assume that a driving term gH_{dr} with an overall amplitude g generates a nonthermal population of doublons and holons. One example of H_{dr} is a resonant optical excitation between the Hubbard bands, as widely adopted in experiments. Another example is the coupling of the system to two separate fermion baths (electrodes), as explained in Methods, and widely used in theoretical studies to emulate the photoexcitation protocol.

We will focus on the strong interaction regime with a weak driving $g \ll t_0 \ll U$ which is nearly resonant with the Mott gap. In this regime one generically finds a stationary nonequilibrium state whose properties are independent of the details of the driving. The system is Mott insulating in equilibrium, and the photodoped carriers have a long lifetime due to the large Mott gap [29–31]. An effective description of the photodoped state can be obtained from a $1/U$ expansion. As $g \ll t_0$, the driving term does not affect H_{eff} to leading order, but it can control the doublon density. Analogous to the doped Mott insulators at equilibrium, the effective physics of the photodoped state is well described by a generalized t-J model [21, 22, 32] $H_{\mathrm{eff}} = H_t + H_J + H_{dh}$ with hopping $H_t = -t_0 \sum_{\langle ij \rangle \sigma} e^{i\varphi_{ij}} [n_{i\bar{\sigma}} c_{i\sigma}^\dagger c_{j\sigma} n_{j\bar{\sigma}} + \bar{n}_{i\bar{\sigma}} c_{i\sigma}^\dagger c_{j\sigma} \bar{n}_{j\bar{\sigma}}] + \mathrm{h.c.}$ and spin exchange $H_J = \sum_{\langle ij \rangle} J_{\mathrm{ex}} \boldsymbol{S}_i \cdot \boldsymbol{S}_j$, where $J_{\mathrm{ex}} = 4t_0^2/U$. We have defined $\bar{n}_{i\bar{\sigma}} = 1 - n_{i,-\sigma}$. The doublon-holon interaction term reads

$$H_{dh} = \frac{J_\perp}{2} \sum_{\langle ij \rangle} (e^{2i\varphi_{ij}} \phi_i^+ \phi_j^- + \mathrm{h.c.}) + J_z \sum_{\langle ij \rangle} \phi_i^z \phi_j^z, \quad (2)$$

where the pairing operators $\phi_i^+ = (\phi_i^-)^\dagger = c_{i\uparrow}^\dagger c_{i\downarrow}^\dagger$ and $\phi_i^z = (n_i - 1)/2$ span a pseudospin $\mathfrak{su}(2)$ algebra similar to that of spin $\boldsymbol{S}_i$. The original model (1) yields $J_\perp = -J_z = J_{\mathrm{ex}}$. The first term in Eq. (2) originates from a doublon-holon exchange process, illustrated in Fig. 1(a), which favors a doublon-holon condensation with $\langle \phi_i^+ \rangle \neq 0$. In solids, the second term is generically renormalized by the intersite Coulomb repulsion which suppresses charge segregation. We will focus in the following on uniform phases with $\langle n_i \rangle = 1$ ($\langle \phi_i^z \rangle = 0$).
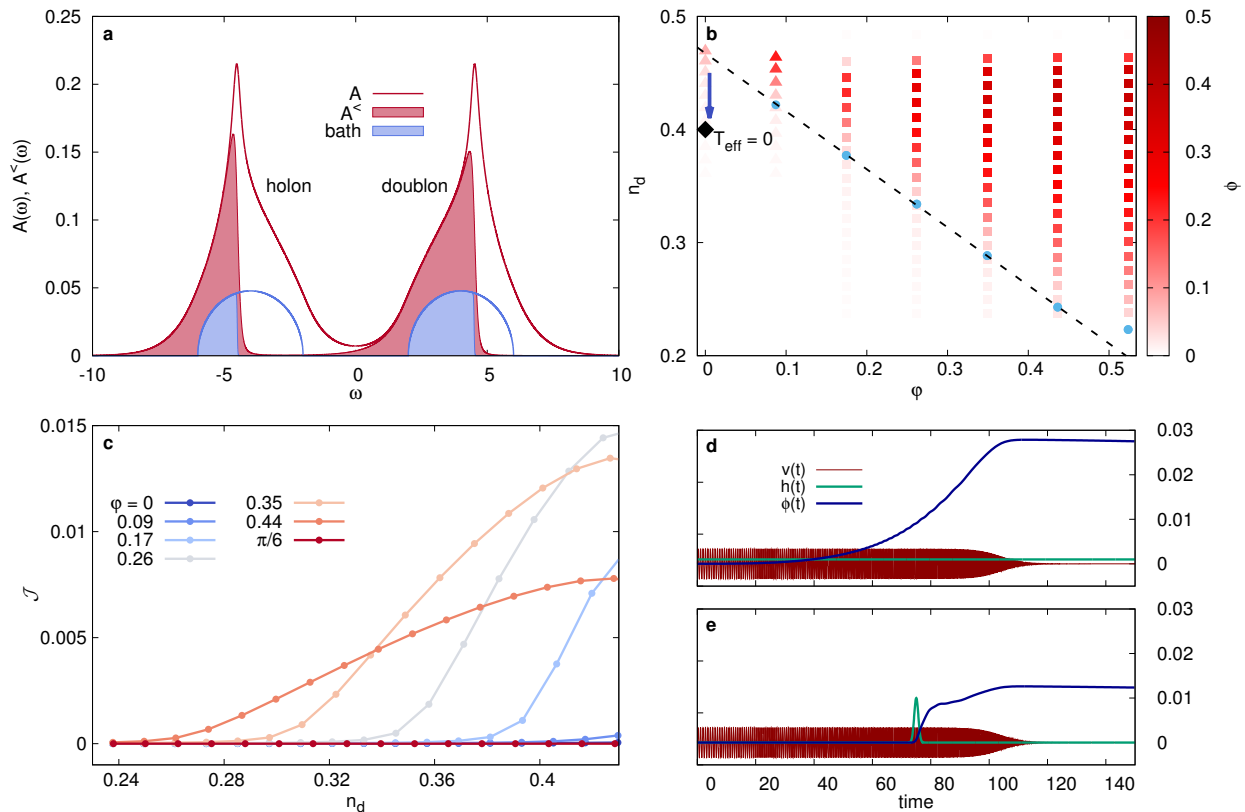
FIG. 2. **The chiral $120°$ condensate on the Bethe lattice.** In panels (a,b,c) the system is driven by two fermion baths, where the "upper" bath injects high-energy electrons to form doublons, while the "lower" bath absorbs low-energy electrons on singly occupied sites to form holons. Panels (d,e) show real-time simulations with an explicit photo-doping pulse. (a) Spectral function and occupation at $\varphi = 0$ for the driven Bethe lattice, with $\mu_b = 4.5, T_b = 0.01, \Gamma = 0.045, U = 8.0$ and bandwidth 4 (in units of t_0). The red-shaded area indicates the occupation of the Hubbard bands, while the blue-shaded area indicates the bath occupation. (b) The n_d–φ phase diagram for the $120°$ condensate sampled by varying the parameters of the fermion baths. The phase φ is in radians and varies from 0 to $\pi/6$. $W = 2$ for the square symbols and $W = 2.7$ for the triangles. The blue dots are obtained by fitting the phase boundary. The black diamond is the extrapolated critical n_d for $T_{\text{eff}} = 0$ and $\varphi = 0$. (c) The persistent current evaluated with $T_b = 0.01, W = 2$. A weak symmetry-breaking field $h = 0.001$ is used in the DMFT iterations. (d) and (e) Transient $120°$-ordered states obtained by means of the entropy cooling protocol for the Bethe lattice with $U = 9.0$ and $\varphi = 0$ using two ways to break the symmetry by a small pair field (green curves $h(t)$). $v(t)$ is the oscillating system-bath coupling which produces the photo-doped state. It is plotted with arbitrary units.

In pump-probe experiments on Mott insulating solids, a strong pump pulse is often applied for a short duration to create a quasi-stationary photodoped state, which can also be described by the above Hamiltonian H_{eff} with $g = 0$. In either set-up, the effective theory for the nonequilibrium state of the Hubbard model is a generalized t-J model of n_d doublons and holons and $n_s = 1 - 2n_d$ unpaired electrons per site.

In this prethermal phase, the positive exchange amplitude $J_\perp$ tends to impose a staggered phase twist for the doublon-holon condensate (η–pairing) [33], but this alternating SC order is generically impossible on a frustrated non-bipartite lattice. Instead, we consider a $120°$ twisted pairing for the three-colorable lattices, defined by $\langle \phi_{i \in R}^+ \rangle = e^{-i2\pi/3} \langle \phi_{i \in G}^+ \rangle = e^{-i4\pi/3} \langle \phi_{i \in B}^+ \rangle = \phi_0$, which spontaneously breaks time-reversal and inversion symmetry. To understand the energetics of the condensate, we can ex-

amine the mean-field energy for the order $\langle \phi_i^+ \rangle = \phi_0 e^{i\boldsymbol{q} \cdot \boldsymbol{r}_i}$ with momentum $\boldsymbol{q}$, given by $\langle H_{dh} \rangle / N_{\text{site}} = |\phi_0|^2 \epsilon(\boldsymbol{q})$ per site, see Supplemental Note 1. In the following, we restrict ourselves to the case $\varphi_{ij} = \varphi$ along each bond of an $R \rightarrow G \rightarrow B$ cycle. For the triangular lattice, the above $120°$ order is of momentum $\boldsymbol{q} = \frac{2\pi}{3}\boldsymbol{b}_1 - \frac{2\pi}{3}\boldsymbol{b}_2$ with reciprocal lattice vectors $\boldsymbol{b}_1, \boldsymbol{b}_2$, and corresponds to one of the two chiral minima of the energy dispersion. This minimum can be further stabilized by an artificial Peierls phase $0 < \varphi < \pi/3$, with $\varphi = \pi/6$ realizing the most stable condensate. The above discussion applies equally to the opposite chirality with a reversed phase twist. The Kagome lattice has three sites in a unit cell, giving rise to three bands in $\epsilon(\boldsymbol{q})$. For $J_\perp > 0$ the lowest-lying band for $J_\perp > 0$ is flat for $\varphi = 0$, which implies that no ordering pattern is singled out as energetically most favorable. The artificial gauge field φ_{ij} can however distort the flat
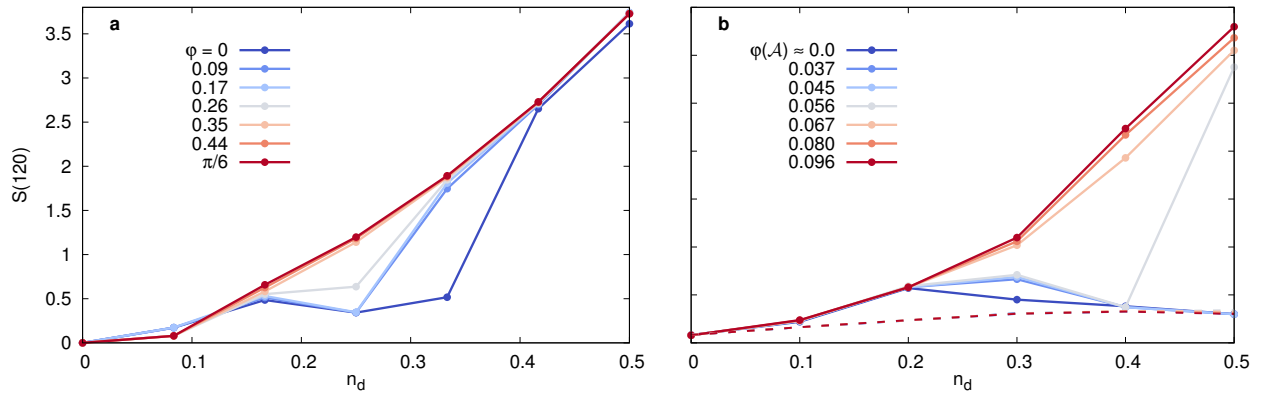
FIG. 3. **Exact diagonalization results for the triangular and Kagome lattices.** (a) The pairing structure factor $S(120)$ of the 120°-twisted condensate versus the doublon number per site n_d for the 12-site triangular lattice at $T_{\text{eff}} = 0$. The Peierls phase φ is varied from 0 to $\pi/6$. (b) The pairing structure factor of the ($\boldsymbol{q} = 0$) 120° order as a function of the doublon density for the 12-site Kagome lattice. The amplitude $\mathcal{A}$ of the dressing field is varied from 0 to 1.4 to produce different φ values, as indicated in the label. Here, an external driving with frequency $\Omega = 5$ is assumed. The dashed line shows the structure factor for the uniform order. $J_\perp = -J_z = 0.5$ is assumed and we impose a spatially homogeneous solution.

band and favor a certain 120° twisted order. As we shall show later in the paper, the order with $\boldsymbol{q} = 0$ illustrated in Fig. 1(c) can be stabilized by an artificial gauge field generated by circularly polarized light.

It remains to be shown that the 120° condensate is stable against quantum fluctuations. We first consider the maximum photodoping situation ($n_d = 0.5$) where all sites are either doubly occupied or empty. In this case $H_{\text{eff}} = H_{dh}$ corresponds to an XXZ model of pseudospin $\boldsymbol{\phi}$. With spatial homogeneity assumed, it is known that the 120° condensate is generically stabilized on the triangular lattice. Furthermore, the 120° condensates constitute the exact ground-state manifold if $J_z = J_\perp \cos(2\pi/3 + \varphi)$ ($J_z = -J_\perp/2$ for $\varphi = 0$, which may be realized with an NN Coulomb repulsion) for both the triangular and Kagome lattices considered here, see Supplemental Note 1 for a proof following the idea of Ref. 34. Away from maximum photodoping, the twisted 120° condensate is challenged by the presence of singly occupied sites, and the additional terms in H_{eff}, such as electron hopping, while the condensate should survive at least for $1/2 - n_d \ll \mathcal{O}(t_0/U)$. We will numerically confirm that this condensate is in fact stable in an extended parameter regime away from the maximum photodoping limit $n_d = 1/2$.

Optical response of the 120° chiral condensate

The twisted 120° condensate embodies a spatially varying phase twist and thus carries a persistent current even in the absence of an external field. With an external vector potential A_{ij} along bond $\langle ij \rangle$, the doublon-holon current contribution along the cycle $R \to G \to B$ is $\mathcal{J}_{ij}^{dh}(A_{ij}) = \delta H_{dh}/\delta A_{ij} \approx 2\mathcal{J}_0^{dh}\sin(2\pi/3 + 2\varphi + 2A_{ij})$ on the mean-field level, where $\mathcal{J}_0^{dh} = -2eJ_1|\phi_0|^2$ with

the elementary charge e. A persistent current $\mathcal{J}_{ij}^{dh}(0) = 2\mathcal{J}_0^{dh}\sin(2\pi/3 + 2\varphi)$ flows even when $A_{ij} = 0$, see arrows in Fig. 1. Indeed, the phase-twisted condensate can be viewed as a frustrated array of Josephson junctions [35].

As usual, a macroscopic superconducting current emerges when the condensate undergoes a uniform electric pulse $\boldsymbol{E}(t)$, which generates a vector potential $\boldsymbol{A}(t) = -\int^t ds \boldsymbol{E}(s)$. However, the breaking of the time-reversal and inversion symmetries allows for a nonlinear and anisotropic supercurrent response, of the general form $\mathcal{J}^a = D^{ab}A_b + T^{abc}A_bA_c + \cdots$ with indices $a, b, c = x/y$ and Einstein convention. This is in contrast to conventional superconductors, where the fully symmetric tensor T^{abc} vanishes due to unbroken inversion or time-reversal symmetries, which imply $\boldsymbol{J}(-\boldsymbol{A}) = -\boldsymbol{J}(\boldsymbol{A})$, and where the London equation $\boldsymbol{J} \propto \boldsymbol{A}$ usually holds.

In particular, the chiral condensate allows for a nonlinear transverse current response perpendicular to $\boldsymbol{A}$, which constitutes a characteristic signature of the symmetry breaking. For the triangular lattice in Fig. 1(b), the three-fold dihedral symmetry (D_3) imposes $T^{xyy} = T^{xxx} = 0$, but allows for nonzero entries obeying $T^{xxy} = -T^{yyy}$. The value of T^{xxy} is determined by evaluating the gauge-invariant supercurrent density $\mathcal{J}^a = \frac{1}{S}\langle \frac{\delta H_{dh}}{\delta A_a} \rangle$ with $a = x, y$ and the total area S. At the mean-field level, one obtains $D^{ab} = \frac{\phi_0^2}{S_{\text{u.c.}}}\frac{\partial^2 \epsilon(\boldsymbol{q}+\boldsymbol{A})}{\partial A_a \partial A_b}$ and $T^{abc} = \frac{\phi_0^2}{2S_{\text{u.c.}}}\frac{\partial^3 \epsilon(\boldsymbol{q}+\boldsymbol{A})}{\partial A_a \partial A_b \partial A_c}$, with the unit-cell area $S_{\text{u.c.}}$, see Supplemental Note 2. Here we consider $\boldsymbol{A}$ along the x–direction. The second-order response emerges due to the trigonal warping $\partial^3 \epsilon/\partial k_x \partial k_x \partial k_y$ of the energy dispersion near the condensation minimum.

The current density is illustrated in Fig. 1(d) and depends strongly on the artificial gauge field φ. In particular, the transverse current vanishes for $\varphi = \pi/6$. The nonlinear and anisotropic response is phenomenologically

similar to the second-order anomalous Hall effect [36, 37] with inversion symmetry breaking, but in contrast to these works, it appears in the context of a SC response and requires the breaking of time-reversal symmetry. It is intriguing to note that if one applies a continuous-wave sinusoidal driving along x ($E_x(t) = E_0 \sin(\omega t)$), the transverse current oscillates at frequency 2ω. This Hall-like response and second-harmonic generation could serve as a smoking gun of the chiral order and can be tested with a four-point measurement.

Numerical determination of the phase diagram

In the remainder of the article, we will explore the phase diagram of the chiral condensate on three different frustrated lattices: the Bethe, the triangular, and the Kagome lattices. To provide a concrete example of the 120° twisted order, we first consider a numerically solvable model in the thermodynamic limit, the driven Hubbard model on the Bethe lattice with hopping $t_0/\sqrt{z}$ where the coordination number is taken to $z \to \infty$. In this case, t_0 is taken as the unit of energy. While this lattice has no loops, the driven system can support the twisted condensate and, most importantly, can be solved using nonequilibrium dynamical mean-field theory (DMFT) in the strong interaction regime [38, 39]. We drive the system by coupling it to two fermion baths with a semielliptic density of states with temperature T_b and different chemical potentials $\pm\mu_b$. As discussed above, the details of the driving do not matter as long as $g \ll t_0$. The baths can be exactly integrated out and incorporated into the DMFT iterations through a hybridization density of states $D_\pm(\epsilon) = \Gamma\sqrt{1 - (\epsilon \pm U/2)^2/W^2}$ with $\Gamma = g^2/W$ and half-bandwidth W. The parameters $\pm\mu_b$ and T_b are varied to control the doublon and holon distribution in the Hubbard system [40].

We show the spectral function $A = -\frac{1}{\pi}\operatorname{Im} G^r$ and the occupation $A^< = \frac{1}{2\pi}\operatorname{Im} G^<$ for a typical driven state in Fig. 2(a). The external driving creates two separate Fermi surfaces in the lower and upper Hubbard bands around $\omega = \pm\mu_b$, indicating the presence of excess doublons and holons. The two Fermi energies correspond to the energy cost or gain associated with the replacement of a doublon or holon by an unpaired electron. Even though the system is highly excited, the Fermi edges can be rather sharp, with low effective temperatures T_{eff} defined by fitting the distribution function $f(\omega) = A^<(\omega)/A(\omega)$ separately near the two Fermi levels. This confirms that the system can be described by a constrained quasi-equilibrium with excess doublons and holons of density n_d and temperature T_{eff}, as already shown in previous works [21, 22, 40]. The order parameter $\phi = \langle \phi^+ \rangle$ is sampled for various bath parameters, which allows to generate the phase diagram for the 120° condensate shown in Fig. 2(b). The system exhibits a transition to the 120°-ordered phase beyond a critical double occupancy n_d^c, indicated by blue dots (see Supplemental Note 3), and is enhanced as φ increases. A persistent current $\mathcal{J}$ flows along $R \to G \to B$, whose magnitude is plotted in panel (c). In experiments, carefully designed protocols can minimze the entropy production and thus achieve low effective temperatures [41]. In our calculations, we can tune the effective temperature of the doublons and holons by changing bath parameters, and then extrapolate the phase boundary to $T_{\text{eff}} = 0$. This procedure yields the upper bound of the critical doublon number $n_d^c \approx 0.4$ at $\varphi = 0$ (black diamond in (b)).

The above results for the Bethe lattice confirm the existence of the 120° SC condensate in a wide parameter range, which extends to $\varphi = 0$ and at least down to $n_d \approx 0.4$, and also the validity of the effective theory (2) at finite U. It remains to be investigated if this intriguing state can be realized on an ultrafast timescale. To address this question, we consider a real-time entropy-cooling protocol [41, 42], which allows to generate cold photodoped states. Here, the system is coupled to two narrow bands with width $W = 0.1$ centered at $\omega = \pm6.0$ and identical chemical potentials $\mu_b = 0$, while the system-bath coupling $v(t)$ oscillates fast to excite photocarriers, see Methods. As shown in Fig. 2(d), a nonzero 120° SC order parameter quickly emerges at $\varphi = 0$ under the driving $v(t)$, in the presence of a small symmetry-breaking field $h = 0.001$ coupling to ϕ_i^+. In the case of transition metal compounds, our unit of time is of the order of femtoseconds. Within the time range accessible in our numerical simulations, the order appears to decay very slowly after the driving is switched off. In addition, we have also simulated a system perturbed by a short pulse of the symmetry-breaking field $h(t)$, see Fig. 2(e). In this case, the 120° order continues to grow after the pulse, which strongly suggests a spontaneous symmetry breaking.

We now use exact diagonalization to directly treat the generalized t-J model (2) on a triangular lattice, to address the existence of the condensate in 2D systems at $T_{\text{eff}} = 0$. We study an $N_{\text{site}} = 12$ cluster with periodic boundary conditions, and calculate the pairing structure factor at the 120° point, namely $S(120) = \sum_{ij} \theta_i \theta_j^* \langle \phi_i^+ \phi_j^- \rangle / N_{\text{site}}$ with $\theta_{i \in R} = e^{i2\pi/3}\theta_{i \in G} = e^{i4\pi/3}\theta_{i \in B} = 1$ corresponding to the "color". $S(120)$ quantifies the total 120° order. The result is shown in Fig. 3(a), and suggests the stability of the 120° condensate away from $n_d = 1/2$ down to $\varphi = 0$, in line with the observation for the Bethe lattice from DMFT. The critical doublon number is $n_d^c(\varphi = 0) \sim 0.37$.

Realization on the Kagome lattice

Finally, we comment on how to realize the 120° SC order on the Kagome lattice. The generalized t-J model

in the maximum photodoping limit ($n_d = 0.5$) is equivalent to an XXZ spin model, which exhibits a complex phase diagram on the Kagome lattice. As discussed above, the key task is to induce an artificial gauge field which favors a specific 120° ordering pattern, for example the $q = 0$ three-coloring of the lattice shown in Fig. 1(c). In the case of solid-state systems, we consider applying a strong laser with circular polarization, similar to the setup in Ref. [27], with a vector potential $\boldsymbol{A}(t) = \mathcal{A}_0(\cos(\Omega t), -\sin(\Omega t))$. The field couples through a time-dependent Peierls phase $\exp(i(\boldsymbol{r}_i - \boldsymbol{r}_j) \cdot \boldsymbol{A}(t))$ to the bond $\langle ij \rangle$. In the high-frequency limit ($\Omega \gg t_0$, off-resonant with U), the hopping parameters are renormalized, leading to a complex nearest-neighbor (NN) hopping $t_R = |t_R|e^{i\varphi(\mathcal{A})}$. This renormalized hopping appears to favor the $q = 0$ condensate shown in Fig. 1(c). The next-nearest neighbor hopping which is also created and would favor a uniform order is usually very small, see the Supplemental Note 4.

We study the resulting effective model on a 12-site cluster with exact diagonalization, defining $\mathcal{A} = \mathcal{A}_0 a/2$ with lattice constant a. The results are shown in Fig. 3(b), and clearly indicate the appearance of the ($q = 0$) 120° SC condensate for $\varphi(\mathcal{A}) \gtrsim 0.067$ and $n_d \gtrsim 0.3$. The dependence of $S(120)$ on n_d is qualitatively similar for both the triangular and Kagome lattices above the transition. In contrast, the uniform order (indicated by the dashed line) is always suppressed. It is worth noting that other orders, such as an $\sqrt{3} \times \sqrt{3}$ type 120° order cannot be studied with the small cluster shown in Fig. 1. The two orders share the identical mean-field energy at $\varphi = 0$. However, a nonzero $|\varphi| < \pi/3$ stabilizes the $q = 0$ order considered here, see Supplemental Note 4. The $\sqrt{3} \times \sqrt{3}$ type order can however be stabilized with a different gauge field, see Supplemental Note 4. Finally we note that other terms, which are generated by the Floquet driving but ignored here, can alter the phase diagram at the quantitative level.

Conclusion

Our work established a new type of chiral superconductivity in photodoped Mott insulators, which breaks the time-reversal and inversion symmetries through a spatially twisted order parameter, namely the 120° condensate. This condensate originates from a positive doublon-holon exchange amplitude $J_\perp > 0$, which is intrinsically related to the nonequilibrium nature of the photodoped states and contrasts with the negative exchange in equilibrium BEC-like pairing induced by charge attraction [43]. The exchange processes furthermore generate a doublon-holon interaction (the J_z term), which favors charge segregation. This effect is ignored here, since it should be suppressed by the inter-site Coulomb repulsion in solids. Also, if the ordered phase is created by an ul-

trafast uniform excitation, we can assume that the state remains homogeneous on the femtoseconds timescale. In the presence of a light-induced artificial gauge field, the order can be further enhanced and even stabilized on the Kagome lattice. The persistent loop current and the nonlinear transverse superconducting current are characteristic signatures of the chiral 120° condensate and allow to realize a second harmonic generation. The phenomenology contrasts with the conventional description of the SC electromagnetic response based on the linear London equation $\boldsymbol{j} \propto \boldsymbol{A}$, where even-order responses are excluded by time-reversal and inversion symmetry.

In experiments, the photodoped state can be realized by applying femtosecond laser pulses to condensed matter systems [7], or via the tilting of optical lattices [44]. When low entropies are maintained, both protocols allow to create long-lived photodoped doublons and holons in the presence of a large Mott gap [29–31], which quickly relax to a prethermal regime characterized by the generalized t-J physics. Since the condensate exists down to $\varphi = 0$, it can be relevant to the photodoped SC states in correlated materials of triangular lattice geometry, such as κ–(BEDT–TTF)$_2$Cu[N(CN)$_2$]Br [12]. Finally, doped Mott insulators have a very rich phase diagram, and the competition between the chiral condensate and other long-lived and hidden phases, especially away from maximum photodoping, is an interesting topic for further investigations.

––––––––––

[1] Kiefl, R. F. *et al.* Search for anomalous internal magnetic fields in high-T_c superconductors as evidence for broken time-reversal symmetry. *Phys. Rev. Lett.* **64**, 2082–2085 (1990). URL https://link.aps.org/doi/10.1103/PhysRevLett.64.2082.

[2] Mackenzie, A. P. & Maeno, Y. The superconductivity of Sr$_2$RuO$_4$ and the physics of spin-triplet pairing. *Rev. Mod. Phys.* **75**, 657–712 (2003). URL https://link.aps.org/doi/10.1103/RevModPhys.75.657.

[3] Joynt, R. & Taillefer, L. The superconducting phases of UPt$_3$. *Rev. Mod. Phys.* **74**, 235–294 (2002). URL https://link.aps.org/doi/10.1103/RevModPhys.74.235.

[4] Avers, K. E. *et al.* Broken time-reversal symmetry in the topological superconductor UPt$_3$. *Nat. Phys.* **16**, 531–535 (2020). URL https://doi.org/10.1038/s41567-020-0822-z.

[5] Cao, Y. *et al.* Superlattice-induced insulating states and valley-protected orbits in twisted bilayer graphene. *Phys. Rev. Lett.* **117**, 116804 (2016). URL https://link.aps.org/doi/10.1103/PhysRevLett.117.116804.

[6] Ichikawa, H. *et al.* Transient photoinduced 'hidden' phase in a manganite. *Nat. Mater.* **10**, 101 (2011). URL https://doi.org/10.1038/nmat2929.

[7] Stojchevska, L. *et al.* Ultrafast switching to a stable hidden quantum state in an electronic crystal. *Science* **344**, 177–180 (2014). URL https://doi.org/10.1126/science.1241591.

[8] de Paz, A. *et al.* Nonequilibrium quantum magnetism in a dipolar lattice gas. *Phys. Rev. Lett.* **111**, 185305 (2013). URL https://link.aps.org/doi/10.1103/PhysRevLett.111.185305.

[9] Singh, K. *et al.* Quantifying and controlling prethermal nonergodicity in interacting floquet matter. *Phys. Rev. X* **9**, 041021 (2019). URL https://link.aps.org/doi/10.1103/PhysRevX.9.041021.

[10] Fausti, D. *et al.* Light-induced superconductivity in a stripe-ordered cuprate. *Science* **331**, 189–191 (2011). URL https://science.sciencemag.org/content/331/6014/189.

[11] Mitrano, M. *et al.* Possible light-induced superconductivity in K_3C_{60} at high temperature. *Nature* **530**, 461 (2016). URL https://doi.org/10.1038/nature16522.

[12] Buzzi, M. *et al.* Photomolecular high-temperature superconductivity. *Phys. Rev. X* **10**, 031028 (2020). URL https://link.aps.org/doi/10.1103/PhysRevX.10.031028.

[13] Budden, M. *et al.* Evidence for metastable photo-induced superconductivity in K_3C_60. *Nat. Phys.* **17**, 611–618 (2021). URL https://doi.org/10.1038/s41567-020-01148-1.

[14] Iwai, S. *et al.* Ultrafast optical switching to a metallic state by photoinduced Mott transition in a Halogen-Bridged Nickel-chain compound. *Phys. Rev. Lett.* **91**, 057401 (2003). URL https://link.aps.org/doi/10.1103/PhysRevLett.91.057401.

[15] Okamoto, H. *et al.* Ultrafast charge dynamics in photoexcited Nd_2CuO_4 and La_2CuO_4 cuprate compounds investigated by femtosecond absorption spectroscopy. *Phys. Rev. B* **82**, 060513 (2010). URL https://link.aps.org/doi/10.1103/PhysRevB.82.060513.

[16] Beaud, P. *et al.* A time-dependent order parameter for ultrafast photoinduced phase transitions. *Nat. Mater.* **13**, 923 (2014). URL https://doi.org/10.1038/nmat4046.

[17] Dean, M. *et al.* Ultrafast energy-and momentum-resolved dynamics of magnetic correlations in the photo-doped Mott insulator Sr_2IrO_4. *Nat. Mater.* **15**, 601 (2016). URL https://doi.org/10.1038/nmat4641.

[18] Ligges, M. *et al.* Ultrafast doublon dynamics in photoexcited $1T$-TaS_2. *Phys. Rev. Lett.* **120**, 166401 (2018). URL https://link.aps.org/doi/10.1103/PhysRevLett.120.166401.

[19] Rosch, A., Rasch, D., Binz, B. & Vojta, M. Metastable superfluidity of repulsive fermionic atoms in optical lattices. *Phys. Rev. Lett.* **101**, 265301 (2008). URL https://link.aps.org/doi/10.1103/PhysRevLett.101.265301.

[20] Peronaci, F., Parcollet, O. & Schiró, M. Enhancement of local pairing correlations in periodically driven Mott insulators. *Phys. Rev. B* **101**, 161101 (2020). URL https://link.aps.org/doi/10.1103/PhysRevB.101.161101.

[21] Li, J., Golez, D., Werner, P. & Eckstein, M. η-paired superconducting hidden phase in photodoped Mott insulators. *Phys. Rev. B* **102**, 165136 (2020). URL https://link.aps.org/doi/10.1103/PhysRevB.102.165136.

[22] Murakami, Y. *et al.* Exploring nonequilibrium phases of photo-doped Mott insulators with generalized Gibbs ensembles. *Commun. Phys.* **5**, 1–8 (2022). URL https://doi.org/10.1038/s42005-021-00799-7.

[23] Kalmeyer, V. & Laughlin, R. B. Equivalence of the resonating-valence-bond and fractional quantum Hall states. *Phys. Rev. Lett.* **59**, 2095–2098 (1987). URL https://link.aps.org/doi/10.1103/PhysRevLett.59.2095.

[24] Struck, J. *et al.* Engineering Ising-XY spin-models in a triangular lattice using tunable artificial gauge fields. *Nat. Phys.* **9**, 738–743 (2013). URL https://doi.org/10.1038/nphys2750.

[25] Struck, J. *et al.* Tunable gauge potential for neutral and spinless particles in driven optical lattices. *Phys. Rev. Lett.* **108**, 225304 (2012). URL https://link.aps.org/doi/10.1103/PhysRevLett.108.225304.

[26] Hauke, P. *et al.* Non-abelian gauge fields and topological insulators in shaken optical lattices. *Phys. Rev. Lett.* **109**, 145301 (2012). URL https://link.aps.org/doi/10.1103/PhysRevLett.109.145301.

[27] Claassen, M., Jiang, H.-C., Moritz, B. & Devereaux, T. P. Dynamical time-reversal symmetry breaking and photo-induced chiral spin liquids in frustrated Mott insulators. *Nat. Commun.* **8**, 1–9 (2017). URL https://doi.org/10.1038/s41467-017-00876-y.

[28] Shores, M. P., Nytko, E. A., Bartlett, B. M. & Nocera, D. G. A structurally perfect S= 1/2 Kagome antiferromagnet. *J. Am. Chem. Soc.* **127**, 13462–13463 (2005). URL https://doi.org/10.1021/ja053891p.

[29] Sensarma, R. *et al.* Lifetime of double occupancies in the fermi-Hubbard model. *Phys. Rev. B* **82**, 224302 (2010). URL https://link.aps.org/doi/10.1103/PhysRevB.82.224302.

[30] Eckstein, M. & Werner, P. Thermalization of a pump-excited Mott insulator. *Phys. Rev. B* **84**, 035122 (2011). URL https://link.aps.org/doi/10.1103/PhysRevB.84.035122.

[31] Mitrano, M. *et al.* Pressure-dependent relaxation in the photoexcited mott insulator ET-F_2TCNQ: Influence of hopping and correlations on quasiparticle recombination rates. *Phys. Rev. Lett.* **112**, 117801 (2014). URL https://link.aps.org/doi/10.1103/PhysRevLett.112.117801.

[32] Kaneko, T., Yunoki, S. & Millis, A. J. Charge stiffness and long-range correlation in the optically induced η-pairing state of the one-dimensional Hubbard model. *Phys. Rev. Research* **2**, 032027 (2020). URL https://link.aps.org/doi/10.1103/PhysRevResearch.2.032027.

[33] Yang, C. N. η pairing and off-diagonal long-range order in a Hubbard model. *Phys. Rev. Lett.* **63**, 2144–2147 (1989). URL https://link.aps.org/doi/10.1103/PhysRevLett.63.2144.

[34] Changlani, H. J., Kochkov, D., Kumar, K., Clark, B. K. & Fradkin, E. Macroscopically degenerate exactly solvable point in the spin-1/2 Kagome quantum antiferromagnet. *Phys. Rev. Lett.* **120**, 117202 (2018). URL https://link.aps.org/doi/10.1103/PhysRevLett.120.117202.

[35] Théron, R., Korshunov, S. E., Simond, J. B., Leemann, C. & Martinoli, P. Observation of domain-wall superlattice states in a frustrated triangular array of Josephson junctions. *Phys. Rev. Lett.* **72**, 562–565 (1994). URL https://link.aps.org/doi/10.1103/PhysRevLett.72.562.

[36] Sodemann, I. & Fu, L. Quantum nonlinear Hall effect induced by Berry curvature dipole in time-reversal invariant materials. *Phys. Rev. Lett.* **115**, 216806 (2015). URL https://link.aps.org/doi/10.1103/PhysRevLett.115.216806.

[37] Nagaosa, N. & Morimoto, T. Concept of quantum geometry in optoelectronic processes in solids: Application to solar cells. *Adv. Mater.* **29**, 1603345 (2017). URL https://doi.org/10.1002/adma.201603345.

[38] Georges, A., Kotliar, G., Krauth, W. & Rozenberg, M. J. Dynamical mean-field theory of strongly correlated fermion systems and the limit of infinite dimensions. *Rev. Mod. Phys.* **68**, 13–125 (1996). URL https://link.aps.org/doi/10.1103/RevModPhys.68.13.

[39] Aoki, H. *et al.* Nonequilibrium dynamical mean-field theory and its applications. *Rev. Mod. Phys.* **86**, 779–837 (2014). URL https://link.aps.org/doi/10.1103/RevModPhys.86.779.

[40] Li, J. & Eckstein, M. Nonequilibrium steady-state theory of photodoped Mott insulators. *Phys. Rev. B* **103**, 045133 (2021). URL https://link.aps.org/doi/10.1103/PhysRevB.103.045133.

[41] Werner, P., Eckstein, M., Müller, M. & Refael, G. Light-induced evaporative cooling of holes in the Hubbard model. *Nat. Commun.* **10**, 1–7 (2019). URL https://doi.org/10.1038/s41467-019-13557-9.

[42] Werner, P., Li, J., Golež, D. & Eckstein, M. Entropy-cooled nonequilibrium states of the Hubbard model. *Phys. Rev. B* **100**, 155130 (2019). URL https://link.aps.org/doi/10.1103/PhysRevB.100.155130.

[43] Micnas, R., Ranninger, J. & Robaszkiewicz, S. Superconductivity in narrow-band systems with local nonretarded attractive interactions. *Rev. Mod. Phys.* **62**, 113–171 (1990). URL https://link.aps.org/doi/10.1103/RevModPhys.62.113.

[44] Greif, D., Tarruell, L., Uehlinger, T., Jördens, R. & Esslinger, T. Probing nearest-neighbor correlations of ultracold fermions in an optical lattice. *Phys. Rev. Lett.* **106**, 145302 (2011). URL https://link.aps.org/doi/10.1103/PhysRevLett.106.145302.

[45] Keiter, H. & Kimball, J. Diagrammatic perturbation technique for the Anderson Hamiltonian, and relation to the sd exchange Hamiltonian. *Int. J. Magnetism* **1**, 233 (1971).

[46] Eckstein, M. & Werner, P. Nonequilibrium dynamical mean-field calculations based on the noncrossing approximation and its generalizations. *Phys. Rev. B* **82**, 115115 (2010). URL https://link.aps.org/doi/10.1103/PhysRevB.82.115115.

[47] Li, J., Golez, D., Werner, P. & Eckstein, M. Superconducting optical response of photodoped Mott insulators. *Mod. Phys. Lett. B* **34**, 2040054 (2020). URL https://doi.org/10.1142/S0217984920400540.

Methods

Nonequilibrium dynamical mean-field theory solution. We solve the driven Hubbard model on the Bethe lattice with infinite coordination number using nonequilibrium dynamical mean-field theory [39]. The model can be exactly mapped to the Anderson model when the hopping is rescaled with $t_0/\sqrt{z}$ and $z \to \infty$ and solvable through dynamical mean-field theory, and thus provides a concrete solvable model to establish the 120° order. This rescaling leads to a noninteracting bandwidth $4t_0$. The exchange interaction for each bond is given by $J_{\mathrm{ex}} = 4t_0^2/zU$, while the total (mean-field) energy contribution scales with z times this value, $4t_0^2/U$. This infinite-coordinational model captures local correlation effects and, in particular, the interplay between hopping and exchange interactions, while it completely neglects nonlocal correlations as well as the effects of electrons hopping around loops, present in lower dimensional systems.

The lattice problem is exactly mapped to three single-impurity Anderson models on the Keldysh contour, defined by the action (spin index neglected for simplicity of notation)

$$
S_{X,\mathrm{imp}} = \int dt c_X^\dagger(t)(i\partial_t - h_{\mathrm{loc}})c_X(t)
$$
$$
- \int dt dt' c_X^\dagger(t)[\Delta_X(t-t') + \sum_\ell D_\ell(t-t')]c_X(t'),
\tag{3}
$$

where $X = R, G, B$ and $\Delta_X(t, t')$ is the total bath hybridization function. For an R site, half of its neighbors are G sites and the other half are B, and similarly for the other two sites. The local Hamiltonian h_{loc} includes the Hubbard interaction and the pair seed term. The self-consistency relation, which is given below, yields Δ from the local Green's function $G_{\mathrm{loc}}(t, t') = G_{\mathrm{imp}}(t, t')$. $D_\pm$ is the bath hybridization. The steady-state problem is solved with a frequency-domain strong-coupling impurity solver, whose implementation is detailed in Ref. [40].

In the nonequilibrium steady-state setup, the driving term reads $gH_{\mathrm{dr}} = \frac{g}{\sqrt{L}} \sum_{i\sigma\alpha}(c_{i\sigma}^\dagger d_{i\alpha\sigma} + \mathrm{h.c.}) + \sum_{i\alpha\sigma} \epsilon_\alpha d_{i\alpha\sigma}^\dagger d_{i\alpha\sigma}$ with bath operators $d_{i\alpha\sigma}$ and $\alpha = (\ell, \xi)$ containing a bath label $\ell = \pm$ and the energy level label ξ. L represents the bath size and is of length dimension. Three impurity problems labelled by R, G, B are solved with the non-crossing approximation (NCA) [45, 46]. In DMFT, the impurity hybridization function is determined by $\Delta_R(t, t') = t_0^2 \tau_z(e^{i\tau_z\varphi}G_B(t, t')e^{-i\tau_z\varphi} + e^{-i\tau_z\varphi}G_G(t, t')e^{i\tau_z\varphi})\tau_z/2$, and analogously for $\Delta_{G/B}$, maintaining a bandwidth of $4t_0$. The Pauli-matrix τ_z appears because of the Nambu formalism [21]. In practice, we apply a seed term $h \sum_i \theta_i c_{i\uparrow}^\dagger c_{i\downarrow}^\dagger + \mathrm{h.c.}$ with $h = 0.001$ to break the symmetry, where $\theta_i = 1, e^{i2\pi/3}, e^{i4\pi/3}$ for the R, G, B site, respectively. The doublon number (per site)

is calculated as $n_d = \langle n_\uparrow n_\downarrow \rangle$.

The real-time dynamics in Fig. 2(d,e) is obtained using the entropy-cooling protocol [41, 42]. To be concrete, the Hubbard system is coupled to two narrow bands at each site, which have a semielliptic DoS of half-bandwidth 0.1 and are located at the energies $\omega_\pm = \pm 6$. The upper (ω_+) band is empty while the lower band (ω_-) is full, as the chemical potential is set to $\mu_b = 0$. We drive the coupling constant $g = v(t)$ with a pulse as given below, inducing a resonant charge transfer between the empty (full) core level and the lower (upper) Hubbard band, respectively. The key idea is to adjust the frequency in time, so as to match the first Floquet sideband of the narrow band with the effective Fermi level for the doublons or holons (roughly speaking one wants $\omega_+ - \Omega(t) \sim \mu_+(t)$, where μ_+ is the Fermi level in the upper Hubbard band, and similarly for the lower Hubbard band). See Ref. 42 for more details. Specifically, the pulse is given by $v(t) = \frac{\sin[\Omega(t)t]}{(1+e^{(t-t_1-T)\gamma_{\mathrm{off}}})(1+e^{-(t-t_1)\gamma_{\mathrm{on}}})}$ for $t > 0$ and zero otherwise, where $\Omega(t) = \Omega_i + (\Omega_f - \Omega_i)\sin(\pi t/400)$ and $t_1 = 4, T = 100, \gamma_{\mathrm{on}} = 1, \gamma_{\mathrm{off}} = 1/4, \Omega_i = 7.25, \Omega_f = 12.5$. The frequency $\Omega(t)$ is varied to fill the upper Hubbard band to its top, and to empty the lower Hubbard band to its bottom. The parameters are empirically optimized to minimize T_{eff} in the final state and generate a long-lived order.

Within DMFT, the current flowing through site R can be calculated by

$$
J = -\frac{1}{2}\,\mathrm{Re}\,\tau_x G_R(t,t') * \Big[t_0^2 \tau_z (e^{i\tau_z\varphi} G_B(t,t') e^{-i\tau_z\varphi}
$$
$$
- e^{-i\tau_z\varphi} G_G(t,t') e^{i\tau_z\varphi})\tau_z/2\Big], \tag{4}
$$

and similarly for the other sites. Here, the symbol $*$ represents a convolution on the Keldysh contour.

Exact diagonalization studies. We solve the generalized t-J model on the triangular and Kagome lattices with the artificial gauge field φ. Three-site terms are ignored, since they play a similar role as the electron hopping, assisting doublon/holon delocalization, but have a much lower strength $J_{\mathrm{ex}} \ll t_0$. Three conserved quan-

tites, the number of up and down spins and the doublon number n_d, are imposed to satisfy $n_\uparrow = n_\downarrow = n_d$. For the triangular lattice, a 12-site cluster, as shown in Fig. 1(b), is solved with the Lanczos algorithm. We define $\boldsymbol{a}_1$ ($\boldsymbol{a}_2$) as in Fig. 1(b), and the torus is spanned by $2\boldsymbol{a}_1 + 2\boldsymbol{a}_2$ and $2\boldsymbol{a}_1 - 4\boldsymbol{a}_2$. The green sites at the left and right bottom corners are not in the cluster, but are identified with sites in the cluster using the periodic boundary conditions. The pairing correlation is averaged over sites, using translational invariance and the structure factor is summed over chiralities (replacing $\theta_i \to \theta_i + \theta_i^*$).

In the case of the Kagome lattice, a 12-site cluster, as shown in Fig. 1(c), is solved with the same method. The uppermost green sites and the rightmost red sites are identified with the lowermost and leftmost sites using periodic boundary conditions, respectively. We consider off-resonant polarized light in the long-wavelength limit. The hopping term along bond $\langle ij \rangle$ is then dressed with the Peierls phase $\exp(i\boldsymbol{r}_{ij} \cdot \boldsymbol{A}(t)) = \exp\big[i(\mathcal{A}_{ij} e^{i\Omega t} + \mathcal{A}_{ij}^* e^{-i\Omega t})\big]$, where $\boldsymbol{r}_{ij} = \boldsymbol{r}_i - \boldsymbol{r}_j$ and $\mathcal{A}_{ij} = \mathcal{A}_0 a e^{i\theta_{ij}}/2$ for the bond with lattice constant a which is parallel to $(\cos\theta_{ij}, \sin\theta_{ij})$.

The lth Fourier component of the Hamiltonian reads

$$
H_l = \delta_{l0} \sum_i U_i n_{i\uparrow} n_{i\downarrow} - i^{|l|} t_0 \sum_{\langle ij \rangle \sigma} e^{il\theta_{ij}} J_{|l|}(\mathcal{A}) c_{i\sigma}^\dagger c_{j\sigma}, \tag{5}
$$

where $\mathcal{A} = \mathcal{A}_0 a/2$ the J_l are Bessel functions of the first kind. In the high-frequency limit, one can obtain the effective Hamiltonian with a $1/\Omega$ expansion,

$$
H_0 + \sum_{l>0}[H_l, H_{-l}]/l\Omega
$$
$$
= \sum_i U_i n_{i\uparrow} n_{i\downarrow} - t_{\mathrm{R}} \sum_{\langle ij \rangle \sigma} c_{i\sigma}^\dagger c_{j\sigma} - t_{\mathrm{NNN}} \sum_{\langle\langle ijk \rangle\rangle \sigma} c_{i\sigma}^\dagger c_{k\sigma}. \tag{6}
$$

The complex NN hopping and purely imaginary next NN hopping read

$$
t_{\mathrm{R}} = t_0 J_0(\mathcal{A}) - i t_0^2 \sum_l (-)^l J_l(\mathcal{A})^2 \sin(2l\pi/3)/l\Omega,
$$
$$
t_{\mathrm{NNN}} = -i t_0^2 \sum_l (-)^l J_l(\mathcal{A})^2 \sin(l\pi/3)/l\Omega. \tag{7}
$$

We include both hoppings in the simulation.

Supplementary Materials

$120°$ twisted superconducting order at maximum photodoping

At maximum photodoping $n_d = 1/2$, the effective Hamiltonian for the half-filled Hubbard model is given by the XXZ model

$$H_{\text{eff}} = \frac{J_\perp}{2} \sum_{\langle ij \rangle} (e^{2i\varphi_{ij}} \phi_i^+ \phi_j^- + \text{h.c.}) + J_z \sum_{\langle ij \rangle} \phi_i^z \phi_j^z, \tag{8}$$

where $\varphi_{RG} = -\varphi_{GR} = (\text{cyclic}) = \varphi$ for uniform phases $\langle \phi_i^z \rangle = 0$. We will investigate the condensate with "momentum" $\boldsymbol{q}$, namely $\langle \phi_i^+ \rangle = \phi_0 e^{i\boldsymbol{q} \cdot \boldsymbol{r}_i}$. On the triangular lattice, the energy per site is given by $\phi_0^2 \epsilon(\boldsymbol{q})$, where the dispersion $\epsilon(\boldsymbol{q})$ reads

$$\epsilon(\boldsymbol{q}) = J_\perp [\cos(q_1 + 2\varphi) + \cos(q_2 - 2\varphi) + \cos(q_2 - q_1 + 2\varphi)]. \tag{9}$$

The $q_{1,2}$ are the reciprocal coordinates, defined as $\boldsymbol{q} = q_1 \boldsymbol{b}_1 + q_2 \boldsymbol{b}_2$, with reciprocal basis vectors $\boldsymbol{b}_1 = (2/\sqrt{3}, 0), \boldsymbol{b}_2 = (-1/\sqrt{3}, 1)$. The energy dispersion $\epsilon(\boldsymbol{q})$ has two minima at $\boldsymbol{q} = \pm[(-2\pi/3)\boldsymbol{b}_1 + 2\pi/3\boldsymbol{b}_2)]$, for $\varphi = 0$, corresponding to two different chiral $120°$ condensates. As φ becomes nonzero, one of the two chiral states becomes the unique minimum in the energy landscape, with a reduced energy in the range $|\varphi| < \pi/3$. The situation for $\varphi > 0$ is illustrated in the left panels of Fig. 4, where the minimum at $(2\pi/3)\boldsymbol{b}_1 + (-2\pi/3)\boldsymbol{b}_2$ is stabilized.

In the case of the Kagome lattice, the energy dispersion splits into three bands because of the three atoms in a unit cell. A flat band emerges as the lowest-lying one at $\varphi = 0$, and thus no particular order is favored. The actual ground state is selected by quantum fluctuations. However, if we impose the φ_{ij} pattern shown in Fig. 1(c), the $\boldsymbol{q} = 0$ order is stabilized as φ increases.

Exactly solvable point

For triangular and Kagome lattices, the Hamiltonian H_{eff} can be decomposed as $H_{\text{eff}} = \sum_\Delta h(\Delta)$, i.e., into a sum of triangular motifs Δ. In the following, we will prove that the $120°$ condensate is the exact ground state for $J_z = J_\perp \cos(2\pi/3 + \varphi)$ and $0 < \varphi < \pi/3$, following the argument of Changlani *et al.* [34]. For simplicity, we use pseudospin $|\uparrow\rangle$ and $|\downarrow\rangle$ to denote doublon and holon states, respectively.

More percisely, we will prove that the coherent state of hard-core doublons

$$|\Psi\rangle = \exp\left(\sum_i \theta_i^* \phi_i^+ \right) |0\rangle \tag{10}$$

is a ground state of the Hamiltonian if $J_z = J_\perp \cos(2\pi/3 + \varphi)$. Here the sum is over all sites i, and the "color" θ_i is defined as in the main text. This state is essentially a tensor-product state $\otimes_i |C_i\rangle$ with $C_i = R, G, B$ at each site i, defined as $|R\rangle = \frac{1}{\sqrt{2}}(|\uparrow\rangle + |\downarrow\rangle), |G\rangle = \frac{1}{\sqrt{2}}(|\uparrow\rangle + \omega |\downarrow\rangle), |B\rangle = \frac{1}{\sqrt{2}}(|\uparrow\rangle + \omega^2 |\downarrow\rangle)$ with $\omega = e^{i2\pi/3}$.

The Hilbert space of each motif is spanned by eight orthogonal states, including the fully polarized $|3/2\rangle = |\uparrow\uparrow\uparrow\rangle, |-3/2\rangle = |\downarrow\downarrow\downarrow\rangle$ and two sets of chiral states defined by

$$\begin{aligned}
|+1/2\rangle_L &= |\downarrow\uparrow\uparrow\rangle + \omega |\uparrow\downarrow\uparrow\rangle + \omega^2 |\uparrow\uparrow\downarrow\rangle, \\
|-1/2\rangle_L &= |\uparrow\downarrow\downarrow\rangle + \omega^2 |\downarrow\uparrow\downarrow\rangle + \omega |\downarrow\downarrow\uparrow\rangle, \\
|+1/2\rangle_R &= |\downarrow\uparrow\uparrow\rangle + \omega^2 |\uparrow\downarrow\uparrow\rangle + \omega |\uparrow\uparrow\downarrow\rangle, \\
|-1/2\rangle_R &= |\uparrow\downarrow\downarrow\rangle + \omega |\downarrow\uparrow\downarrow\rangle + \omega^2 |\downarrow\downarrow\uparrow\rangle,
\end{aligned} \tag{11}$$

and two nonchiral states

$$\begin{aligned}
|+1/2\rangle_0 &= \frac{1}{\sqrt{3}} (|\downarrow\uparrow\uparrow\rangle + |\uparrow\downarrow\uparrow\rangle + |\uparrow\uparrow\downarrow\rangle) \\
|-1/2\rangle_0 &= \frac{1}{\sqrt{3}} (|\uparrow\downarrow\downarrow\rangle + |\downarrow\uparrow\downarrow\rangle + |\downarrow\downarrow\uparrow\rangle).
\end{aligned} \tag{12}$$
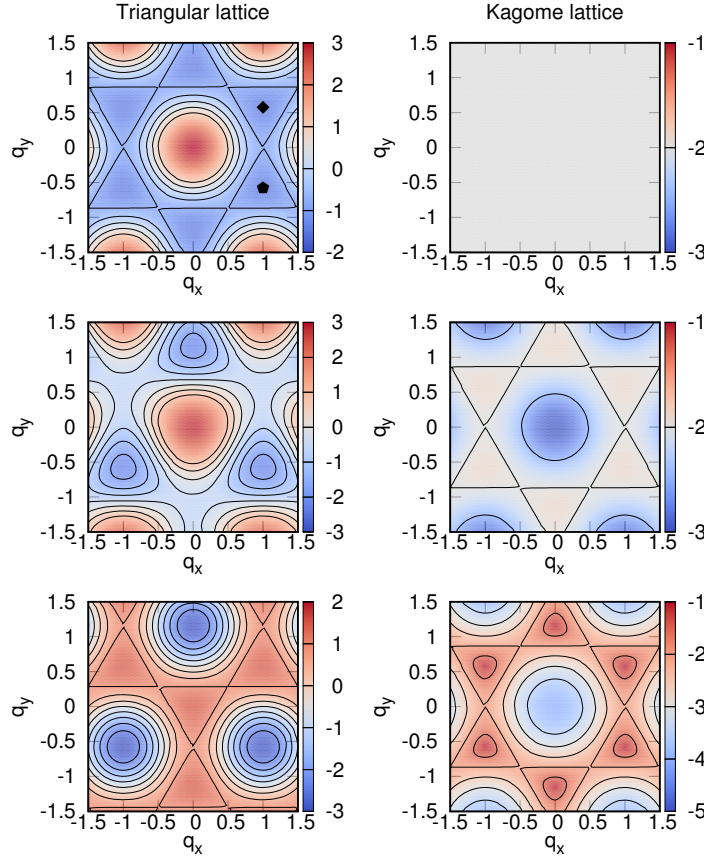
FIG. 4. The energy dispersion $\epsilon(\boldsymbol{q})$ for orders with momentum $\boldsymbol{q}$ on the triangular and the Kagome lattices with $\varphi = 0, \pi/20, \pi/6$ in the first, second, and third row, respectively. Note that the $q_{x,y}$ axes are the cartesian coordinates in the reciprocal space and have units of $2\pi/\sqrt{3}a$. The left panels show the energy dispersion for the triangular lattice. The top panel shows two minima at $\boldsymbol{q} = \pm[(2\pi/3)\boldsymbol{b}_1 + (-2\pi/3)\boldsymbol{b}_2]$, which are degenerate for $\varphi = 0$ and marked by a black pentagon and diamond, respectively. One minimum, $\boldsymbol{q} = (2\pi/3)\boldsymbol{b}_1 + (-2\pi/3)\boldsymbol{b}_2$ (diamond), is selectively stabilized for $0 < \varphi < \pi/3$. For $\varphi = \pi/6$ the stabilization is optimal, and the dispersion becomes nearly isotropic around the minimum, leading to the absence of leading-order trigonal warping and thus to the vanishing of the second-order supercurrent response. The right panels show the lowest-lying band of the Kagome lattice. For $\varphi = 0$ the band is flat, while $\varphi > 0$ stabilizes the $\boldsymbol{q} = 0$ mode.

The above states are labelled by the total z-pseudospin ϕ^z (number of doublons) and the momentum $\pm 2\pi/3, 0$ associated with the three-fold rotational symmetry. It is crucial to note that $|\pm\rangle_L$ are degenerate and $|\pm\rangle_R$ are degenerate due to the symmetry under a combined reflection and a particle-hole transformation (the exchange of $|\uparrow\rangle$ and $|\downarrow\rangle$). Indeed, the above six states are all eigenstates of the Hamiltonian with eigenvalues $\lambda_{\frac{3}{2},0} = \lambda_{-\frac{3}{2},0} = 3J_z/4, \lambda_{\frac{1}{2},L} = \lambda_{-\frac{1}{2},L} = -J_z/4 + J_\perp \cos(2\pi/3 + 2\varphi), \lambda_{\frac{1}{2},R} = \lambda_{-\frac{1}{2},L} = -J_z/4 + J_\perp \cos(2\pi/3 - 2\varphi)$ and $\lambda_{\frac{1}{2},0} = \lambda_{-\frac{1}{2},0} = -J_z/4 + J_\perp \cos(2\varphi)$, where we have labelled the eigenvalues by $\lambda_{\phi_{\text{tot}}^z,c}$ with chirality $c = R, L, 0$. We can verify this by explicit calculations. For $|\pm\rangle_L$ one has

$$
\begin{aligned}
h(\Delta)|+1/2\rangle_L &= e^{-i2\varphi}|\uparrow\downarrow\uparrow\rangle + e^{i2\varphi}|\uparrow\uparrow\downarrow\rangle + e^{-i2\varphi}\omega|\uparrow\uparrow\downarrow\rangle + e^{i2\varphi}\omega|\downarrow\uparrow\uparrow\rangle + e^{-i2\varphi}\omega^2|\downarrow\uparrow\uparrow\rangle + e^{i2\varphi}\omega^2|\uparrow\downarrow\uparrow\rangle \\
&= \lambda_{\frac{1}{2},L}|+1/2\rangle_L \\
h(\Delta)|-1/2\rangle_L &= e^{i2\varphi}|\downarrow\uparrow\downarrow\rangle + e^{-i2\varphi}|\downarrow\downarrow\uparrow\rangle + e^{i2\varphi}\omega^2|\downarrow\downarrow\uparrow\rangle + e^{-i2\varphi}\omega^2|\uparrow\downarrow\downarrow\rangle + e^{i2\varphi}\omega|\uparrow\downarrow\downarrow\rangle + e^{-i2\varphi}\omega|\downarrow\uparrow\downarrow\rangle \\
&= \lambda_{-\frac{1}{2},L}|-1/2\rangle_L,
\end{aligned}
\tag{13}
$$

which are similar for the chiral pairs. The single-motif Hamiltonian $h(\Delta)$ can then be recast into the following form,

$$
H = \sum_\Delta h(\Delta) = \lambda_{\frac{1}{2},0}\sum_\Delta \mathcal{P}_0(\Delta) + \lambda_{\frac{1}{2},R}\sum_\Delta \mathcal{P}_R(\Delta) + \lambda_{\frac{1}{2},L}\sum_\Delta \mathcal{P}_L(\Delta) + \lambda_{\frac{3}{2}}\sum_\Delta \mathcal{P}_{3/2}(\Delta),
\tag{14}
$$

where $\mathcal{P}_{0,R,L,3/2}$ projects the states to the nonchiral, R, L, and fully polarized subspaces for a triangle Δ, respectively. When $J_z = J_\perp \cos(2\pi/3 + 2\varphi)$, the fully polarized states and one set of chiral states $|+1/2\rangle_L$ and $|-1/2\rangle_L$ are degenerate

as $\lambda_{\frac{1}{2},L} = \lambda_{\frac{3}{2}}$. For $0 < \varphi < \pi/3$, the states of the opposite chirality and the nonchiral states lie higher in the energy spectrum of $h(\Delta)$.

A key observation is that, for a single triangular motif, the three-coloring state reads

$$
\begin{aligned}
|R\rangle |G\rangle |B\rangle &= \frac{1}{2^{3/2}} \left[|+3/2\rangle + |-3/2\rangle + (|\uparrow\downarrow\downarrow\rangle + \omega^2 |\downarrow\uparrow\downarrow\rangle + \omega |\downarrow\downarrow\uparrow\rangle) + (|\downarrow\uparrow\uparrow\rangle + \omega |\uparrow\downarrow\uparrow\rangle + \omega^2 |\uparrow\uparrow\downarrow\rangle) \right] \\
&= \frac{1}{2^{3/2}} \left[|3/2\rangle + |-3/2\rangle + |+1/2\rangle_L + |-1/2\rangle_L \right],
\end{aligned}
\tag{15}
$$

which only contains fully polarized states and $|\pm 1/2\rangle_L$. As a result, at $J_z = J_\perp \cos(2\pi/3 + 2\varphi)$, the coherent state $|\Psi\rangle$ consistently zeros out $\mathcal{P}_R$ and $\mathcal{P}_0$, and must be a ground state with energy $3J_z N_\Delta/4$, where N_Δ is the number of triangular motifs.

This three-coloring state is an exact ground state for all ϕ^z sectors, thus equally favoring the 120° condensate and charge segregation (uniform ϕ^z). For the triangular lattice, when $|J_z| < |J_\perp \cos(2\pi/3 + 2\varphi)|$ one can argue that the 120° order is favored. This parameter regime is probably most realistic in experiments due to the intersite Coulomb repulsion. We note that a relatively strong nearest-neighbor Coulomb repulsion $V \sum_{\langle ij \rangle} n_i n_j$ can change J_z to $J_z = V - 4t_0^2/(U - V) > 0$, favoring charge-density-wave order, which is frustrated on the lattices considered here.

The stability against deviations from maximum photodoping ($n_d = 1/2$) has been numerically studied in the main text. At $\varphi = \pi/6$, since the order commutes with the electron-hopping operator, one expects an extended range of stable 120° condensate, at least when the energy scale of the hopping $n_s t_0$ is not much stronger than the exchange energy $J_{\text{ex}} \sim 4t_0^2/U$, namely $n_s = 1 - 2n_d \lesssim 4t_0/U$.

Superconducting optical response

The doublon-holon condensate generally coexists with unpaired electrons, resulting in a gapless state with a large metallic conductivity and negative AC conductivity [47]. The superconducting current response, however, comes from the doublon-holon contribution, which can be expressed as $\mathcal{J}_{ij}^{dh} = \delta H_{dh}[\boldsymbol{A}]/\delta A_{ij} = i2J_\perp (e^{2i(\varphi_{ij} + A_{ij})} \phi_i^+ \phi_j^- - \text{h.c.})$.

For the triangular lattice, we now calculate the currents in the topmost triangular motif shown in Fig. 1(b). We assume that an electric pulse $\boldsymbol{E}(t)$ is applied up to time t_f and $\varphi_{ij} = \varphi$ for a $B \to G \to R$ chain. When $t > t_f$, a constant vector potential $\boldsymbol{A} = -\int^{t_f} \boldsymbol{E}(s)ds$ has been generated and couples to the doublon-holon condensate. Assuming $\boldsymbol{A} = (A_x, A_y)$, we calculate $A_{ij} = \boldsymbol{A} \cdot (\boldsymbol{r}_i - \boldsymbol{r}_j)$ for the three bonds $\langle ij \rangle$ in the topmost triangular motif in Fig. 1(b),

$$
\begin{aligned}
A_{RG} &= \frac{1}{2} A_y - \frac{\sqrt{3}}{2} A_x, \\
A_{GB} &= \frac{1}{2} A_y + \frac{\sqrt{3}}{2} A_x, \\
A_{BR} &= -A_y,
\end{aligned}
\tag{16}
$$

where the lattice constant is set to unity. The three currents then read $\mathcal{J}_{ij} = \mathcal{J}^{dh}(A_{ij})$ for bond index RG, GB, and BR.

In general, we can express the current density as $\mathcal{J}^a = D^{ab} A_b + T^{abc} A_b A_c$ for $a, b, c = x/y$. The form of the coefficient tensors D and T is constrained by symmetry arguments. First of all, any rotational symmetry C_n with $n \geq 3$ requires $D^{ab} \propto \delta^{ab}$, since its faithful 2D representations are irreducible. Moreover, the 120° condensate is invariant under reflection with respect to the y axis, resulting in $T^{xyy} = T^{xxx} = T^{yxy} = 0$. The invariance under the three-fold rotation further imposes $-T^{yyy} = T^{yxx} = T^{xxy}$.

We now concentrate on the bulk response of the triangular lattice. Note that the gauge-invariant current density generally reads $\boldsymbol{J} = \delta H/\delta \boldsymbol{A}$. On the mean-field level, the expectation value of the Hamiltonian per unit cell can be written as

$$
\frac{\langle H \rangle}{N_{\text{site}} S_{\text{u.c.}}} = \frac{\epsilon(\boldsymbol{q}_0 + \boldsymbol{A})}{S_{\text{u.c.}}} = \frac{J_\perp \phi_0^2}{S_{\text{u.c.}}} [\cos(2\pi/3 + 2\varphi + 2A_{RG}) + \cos(2\pi/3 + 2\varphi + 2A_{GB}) + \cos(2\pi/3 + 2\varphi + 2A_{BR})],
\tag{17}
$$

where $\boldsymbol{q}_0 = (2\pi/3, -2\pi/3)$ and the area of the unit cell is $S_{u.c.} = \sqrt{3}/2$. The energy stationarity guarantees that the net current density $\propto \partial\epsilon/\partial\boldsymbol{A}$ vanishes. The linear response is then determined by the concavity $D^{ab} \propto \partial^2\epsilon/\partial A_a \partial A_b$ and the second-order response can be attributed to the trigonal warping $T^{abc} \propto \partial^3\epsilon/\partial A_a \partial A_b \partial A_c$.

To obtain some physical insights, we calculate explicitly the current density,

$$
\begin{aligned}
\mathcal{J}_x &= \frac{\partial \epsilon(\boldsymbol{A})}{\partial A_x} \frac{1}{S_{\text{u.c.}}} = \mathcal{J}_{GB} - \mathcal{J}_{RG}, \\
\mathcal{J}_y &= \frac{\partial \epsilon(\boldsymbol{A})}{\partial A_y} \frac{1}{S_{\text{u.c.}}} = (\mathcal{J}_{RG} + \mathcal{J}_{GB} - 2\mathcal{J}_{BR})/\sqrt{3}.
\end{aligned}
\tag{18}
$$

These results can also be obtained by calculating the charge passing through a line perpendicular to the x- and y-directions per unit time and length. By expanding the above formula to second order, we obtain

$$
\begin{aligned}
\mathcal{J}_x &\approx \left.\frac{\partial \mathcal{J}^{dh}}{\partial A}\right|_{\boldsymbol{A}=0} \sqrt{3} A_x + \left.\frac{\partial^2 \mathcal{J}^{dh}}{\partial A^2}\right|_{\boldsymbol{A}=0} \frac{\sqrt{3}}{2} A_x A_y, \\
\mathcal{J}_y &\approx \left.\frac{\partial \mathcal{J}^{dh}}{\partial A}\right|_{\boldsymbol{A}=0} \sqrt{3} A_y + \left.\frac{\partial^2 \mathcal{J}^{dh}}{\partial A^2}\right|_{\boldsymbol{A}=0} \frac{\sqrt{3}}{4} (A_x^2 - A_y^2).
\end{aligned}
\tag{19}
$$

When $A_y = 0$, one can see that $\mathcal{J}_x \propto A_x$ while $\mathcal{J}_y$ does not vanish but is proportional to A_x^2. This gives rise to a second-order transverse current when $\boldsymbol{A} = (A_x, 0)$. The D and T tensors are

$$
\begin{aligned}
D^{xx} &= D^{yy} = 2\sqrt{3} J_0^{dh} \cos(2\pi/3 + 2\varphi), \\
T^{yxx} &= -T^{yyy} = T^{xxy} = -\frac{\sqrt{3}}{2} J_0^{dh} \sin(2\pi/3 + 2\varphi),
\end{aligned}
\tag{20}
$$

from which one sees that the T tensor vanishes for $\varphi = \pi/6$. The vanishing of the second-order response can be intuitively seen from Fig. 4, where the energy dispersion near the minimum becomes nearly isotropic which forbids a nonzero third-order derivative.

For the $\boldsymbol{q} = 0$ order on the Kagome lattice, the pulse-induced supercurrent can become unbalanced and result in charge redistribution and thus an oscillation in the order parameter. For example, assuming $A_y = 0, A_x \neq 0$, the Blue site of the bottom left triangular motif in Fig. 7(a) has two incoming currents $\mathcal{J}^{dh}(-\sqrt{3}A_x/2) + \mathcal{J}^{dh}(\sqrt{3}A_x/2)$ and two outgoing $\mathcal{J}^{dh}(0) + \mathcal{J}^{dh}(0)$, differing by $\frac{\partial^2 \mathcal{J}}{\partial A^2} 3A_x^2/4$. Hence, an oscillation in the order parameter and the current is expected to be induced in this system. The $\sqrt{3} \times \sqrt{3}$ order, however, features a similar current response to the triangular lattice.

Phase boundary and the critical doublon number for the Bethe lattice

In this section, we show the fitting of the phase boundary and the effective temperature. The left panel of Fig. 5 plots the order parameter as a function of n_d, which is varied by changing the bath chemical potential μ_b. The data are fitted by dashed lines near the phase transition, and the critical doublon densities n_d^c are estimated as the vanishing points of the dashed lines. The transition is not sharply defined because of the weak symmetry-breaking field $h = 0.001$ introduced in the DMFT iterations. For $W = 2$, the effective temperature in the steady-state setup dramatically shoots up for $n_d \gtrsim 0.43$, resulting in a strongly suppressed order parameter, and the phase boundary cannot be precisely determined in the above way. In this regime, both the external fermion baths and the upper/lower Hubbard bands of the system become close to full or empty, leading to a bottleneck for the thermalization and energy dissipation. This bottleneck can be partially overcome by using $W = 2.7$. However, the intraband thermalization is generically reduced for a nearly full/empty band.

We have also varied T_b to obtain stationary states with different T_{eff}, yielding a function $n_d^c(\varphi, T_{\text{eff}})$. The T_{eff} generally varies along each curve for fixed φ, and as a conservative estimate, we have used the lowest value for $\varphi > 0.09$ for all data points (see the horizontal line in the right panel of Fig. 5). This is a crude approximation which tends to underestimate T_{eff}, and it thus guarantees that we get an *lower bound* for the order paramter at a given T_{eff}. The function $n_d^c(\varphi)$ is determined in the same way for each data set with different T_b. We have not fitted the n_d^c for $\varphi = 0$ and $\varphi = 0.09$, since the order parameters are substantially smaller in these two cases and the fit becomes less robust.

To estimate the critical doublon density at $T_{\text{eff}} = 0$ and $\varphi = 0$, we first fit the curves $n_d^c(\varphi, T_{\text{eff}})$ for each T_b (with the estimated T_{eff}) and extrapolate to obtain an estimate of $n_d^c(0, T_{\text{eff}})$, see the left panel of Fig. 6. The n_d^c data points for varying φ and $T_b = 0.01$ have been shown in Fig. 2, and we can see that the fitted $n_d^c(0)$ is consistent with the data for $\varphi = 0$ and $W = 2.7$. We then extrapolate the function $n_d^c(0, T_{\text{eff}})$ to $T_{\text{eff}} = 0$, as shown in the right panel of Fig. 6.
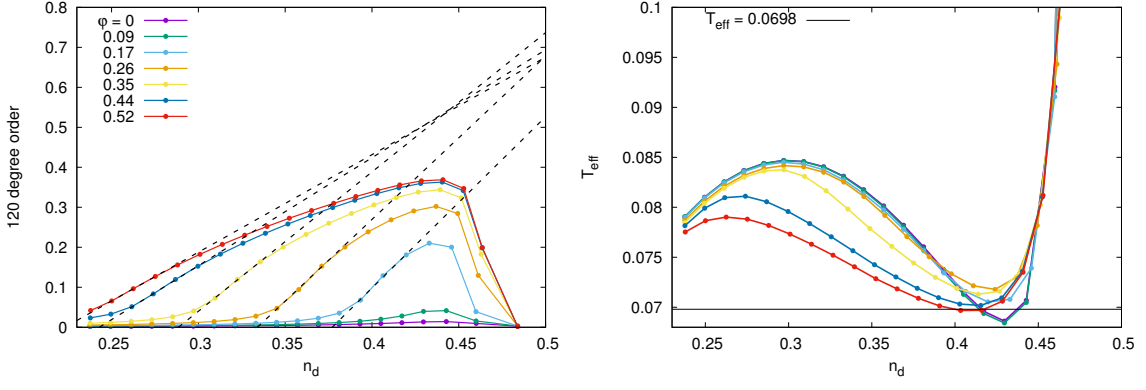
FIG. 5. Determination of the phase boundary by fitting the order parameter (left panel) and the effective temperature for $T_b = 0.01$, $W = 2$ (right panel). The effective temperature is estimated as the minimum of the curves with $\varphi > 0.09$
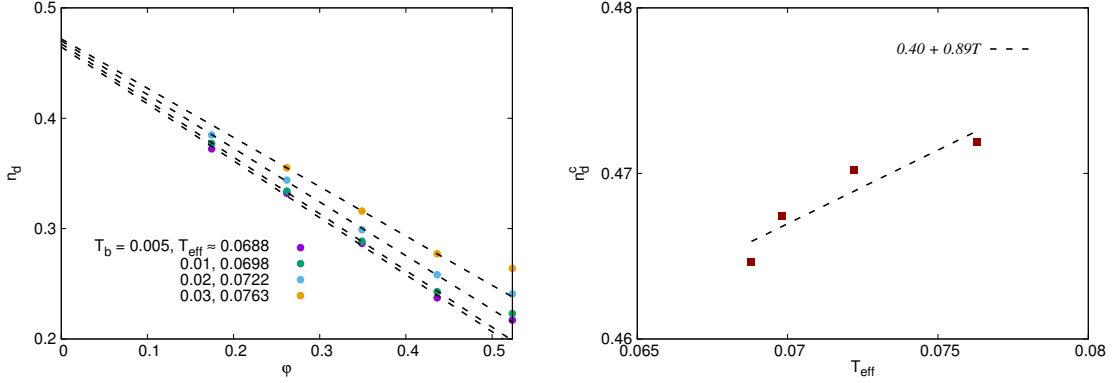
FIG. 6. Fitting of the phase boundary and temperature effects. The data are obtained by varying T_b and the corresponding T_{eff} is estimated as in the text. The fermion bath has $W = 2$. The left panel shows fits of the phase boundary which are extrapolated to $\varphi = 0$. The extrapolated $\varphi = 0$ critical doublon number is consistent with the order parameter obtained with the $W = 2.7$ bath. The right panel shows the extrapolated $n_d(\varphi = 0)$ as a function of T_{eff}. From these values we can obtain the rather conservative upper bound $n_d \approx 0.40$ at $T_{\text{eff}} \to 0$.

The driven Hubbard model on the Kagome lattice

Floquet driving with a circularly polarized light creates a complex phase for the hopping parameter t_R up to the lowest order in a $1/\Omega$ expansion. In fact, it adds to the original t_0 a purely imaginary term at the order t_0^2 (see Methods). The resulting doublon-holon exchange term is of order $t_R^2/U \sim t_0^2/U + \mathcal{O}(t_0^3/U)$. Other terms generated by the light are of higher orders, including a purely imaginary next NN hopping at the order of t_0^2, and thus an exchange term of $\mathcal{O}(t_0^4/U)$. Therefore, we believe the main effect is from the renormalization of t_R. We also note that some Floquet-generated terms, such as the chiral spin interaction proportional to $\boldsymbol{S}_i \cdot (\boldsymbol{S}_j \times \boldsymbol{S}_k)$ [27] can nevertheless alter the phase diagram of the system at the quantitative level.

In this section, we compare the mean-field energy of the uniform, the $\boldsymbol{q} = 0$ and the $\sqrt{3} \times \sqrt{3}$ phases under various driving amplitudes $\mathcal{A}$, see Fig. 7. Specifically, we assume $\phi_0 = 1/2$ and evaluate the doublon-holon interaction term with a mean-field decoupling $\langle \phi_i^+ \phi_i^- \rangle \to \phi_0^2 \theta_i \theta_j^*$, where θ_i is defined as in the pairing structure factor. It suffices to calculate and compare the mean-field energy for a single hexagon. The driving-induced NN and NNN hoppings are shown in Fig. 8(a) and the corresponding mean-field energies are shown in panel (b). The $\boldsymbol{q} = 0$ 120° order has the lowest energy among the three orders, consistent with the ED results shown in the main text.
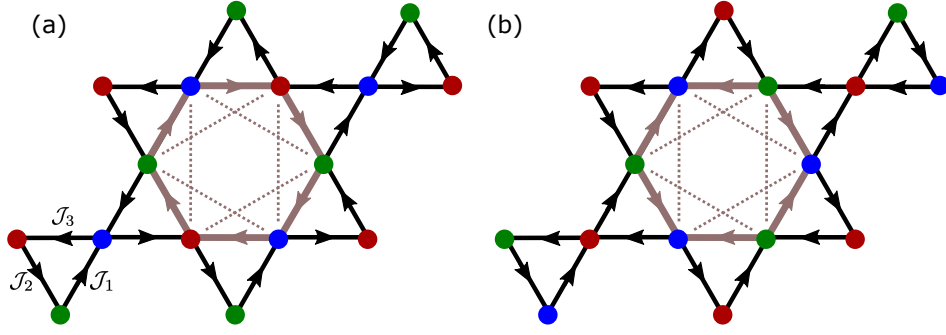
FIG. 7. Hubbard model on the Kagome lattice engineered by circularly polarized laser driving. The NN hopping is renormalized. The induced (second-order in t_0) next NN hopping is shown for one (light-brown) hexagon. (a) When the NN hopping t_R has a phase close to $\pi/6$, it favors the $\boldsymbol{q} = 0$ order. (b) The next-nearest neighbor hopping favors identical order parameters on sites connected by the NNN bond, possibly favoring the uniform order or the $\sqrt{3} \times \sqrt{3}$ order shown here.
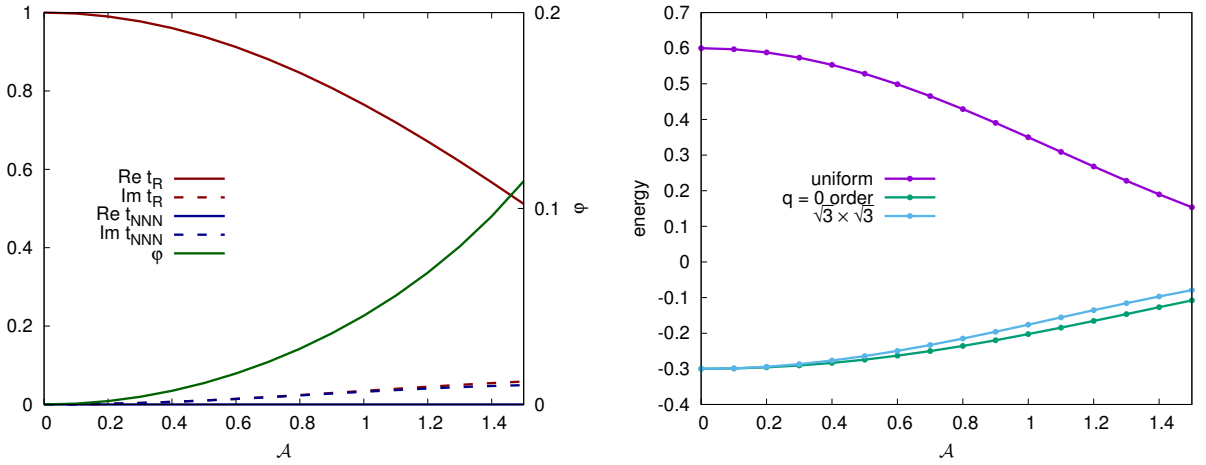
FIG. 8. The hopping parameters (left panel) and semiclassical energy (right panel) for different orders under driving, with $|\phi| = 0.5$ assumed. The parameters are $U/t_0 = 8, \Omega/t_0 = 5$. The $\boldsymbol{q} = 0$ mode generally has the lower energy than the $\sqrt{3} \times \sqrt{3}$ state. In the strong driving limit, the phase of t_R approaches $\pi/2$, and the uniform order becomes significantly enhanced.